fluxes and uncertainties reported here are the error-weighted average of all EPIC detectors.

21. Column (106), LX: logarithm of rest-frame observed 2–10 keV X-ray luminosity (in erg s^{-1}) after correcting for Galactic absorption.
22. Column (107), CHANDRA_SOURCE: the catalog origin of the nearest Chandra source within 10″. An entry of "1" stands for the CDF-S catalog (Luo et al. 2017), "2" stands for the E-CDF-S catalog (Xue et al. 2016), and "3" stands for the CSC 2.0 catalog.
23. Column (108), CHANDRA_ID: Chandra source ID.
24. Columns (109)–(110), CHANDRA_RA, CHANDRA_DEC: R.A. and decl. (in degrees) of the matched Chandra counterpart.

Multiwavelength properties

Columns (111)–(207) provide the multiwavelength properties of the matched counterparts with MATCH_FLAG = 1 utilizing NWAY.

1. Column (111), P_ANY: the posterior probability of the X-ray source having any correct counterparts (p_{any}).
2. Column (112), P_I: the relative probability (p_i) of the reported MATCH_FLAG = 1 counterpart to be the correct match.
3. Column (113), FLAG_SECOND: warning flag for sources where a second possible counterpart is indicated by NWAY.
4. Columns (114)–(121), IRAC_RA, IRAC_DEC, VIDEO_RA, VIDEO_DEC, HSC_RA, HSC_DEC, DES_RA, DES_DEC: R.A. and decl. of the counterpart in the DeepDrill/VIDEO/HSC/DES catalog in degrees. Note that DES counterparts are only reported in areas lacking HSC coverage.
5. Columns (122)–(125), SEP_IRAC, SEP_VIDEO, SEP_HSC, SEP_DES: separation of the X-ray position from the DeepDrill/VIDEO/HSC/DES counterpart in arcseconds.
6. Columns (126)–(129), IRAC_1_MAG, IRAC_1_MAG_ERR, IRAC_2_MAG, IRAC_2_MAG_ERR: 1.9″ aperture photometry and uncertainties in the IRAC 3.6 μm and 4.5 μm bands reported in the DeepDrill catalog.
7. Columns (130)–(139), VIDEO_Z_MAG, VIDEO_Z_MAG_ERR, VIDEO_Y_MAG, VIDEO_Y_MAG_ERR, VIDEO_J_MAG, VIDEO_J_MAG_ERR, VIDEO_H_MAG, VIDEO_H_MAG_ERR, VIDEO_KS_MAG, VIDEO_KS_MAG_ERR: VIDEO 2″ aperture photometry and uncertainties in the *Z*, *Y*, *J*, *H*, and K_s bands.
8. Columns (140)–(147), HSC_G_MAG, HSC_G_MAG_ERR, HSC_R_MAG, HSC_R_MAG_ERR, HSC_I_MAG, HSC_I_MAG_ERR, HSC_Z_MAG, HSC_Z_MAG_ERR: HSC CModel photometry and uncertainties in the *g*, *r*, *i*, and *z* bands.
9. Columns (148)–(157), DES_G_MAG, DES_G_MAG_ERR, DES_R_MAG, DES_R_MAG_ERR, DES_I_MAG, DES_I_MAG_ERR, DES_Z_MAG, DES_Z_MAG_ERR, DES_Y_MAG, DES_Y_MAG_ERR: DES Kron magnitude and uncertainties in the *g*, *r*, *i*, *z*, and *Y* bands.
10. Column (158), TRACTOR_ID: the object ID of the VIDEO counterpart in the forced-photometry catalog (K. Nyland et al. 2021, in preparation).
11. Columns (159)–(188), IRAC_1_FP_MAG, IRAC_1_FP_MAG_ERR, IRAC_2_FP_MAG, IRAC_2_FP_MAG_ERR, VIDEO_Z_FP_MAG, VIDEO_Z_FP_MAG_ERR, VIDEO_Y_FP_MAG,VIDEO_Y_FP_MAG_ERR, VIDEO_J_FP_MAG, VIDEO_J_FP_MAG_ERR, VIDEO_H_FP_MAG, VIDEO_H_FP_MAG_ERR, VIDEO_KS_FP_MAG, VIDEO_KS_FP_MAG_ERR, HSC_G_FP_MAG, HSC_G_FP_MAG_ERR, HSC_R_FP_MAG, HSC_R_FP_MAG_ERR, HSC_I_FP_MAG, HSC_I_FP_MAG_ERR, HSC_Z_FP_MAG, HSC_Z_FP_MAG_ERR, VOICE_U_FP_MAG, VOICE_U_FP_MAG_ERR, VOICE_G_FP_MAG, VOICE_G_FP_MAG_ERR, VOICE_R_FP_MAG, VOICE_R_FP_MAG_ERR, VOICE_I_FP_MAG, VOICE_I_FP_MAG_ERR: forced photometry and uncertainties of DeepDrill 3.6 μm and 4.5 μm bands, VIDEO *ZYJHK*$_s$ bands, HSC *griz* bands, and VOICE *ugri* bands reported in the forced-photometry catalog (K. Nyland et al. 2021, in preparation).
12. Column (189), SPECZ: spectroscopic redshift adopted for the X-ray source.
13. Column (190), SPECZ_CLASS: spectroscopic classification of the source. "1" stands for BL AGNs; "0" stands for galaxies or non-BL AGNs; "−1" stands for stars.
14. Column (191), SPECZ_Q: spectroscopic quality flag of the source reported in the original catalog.
15. Columns (192)–(193), SPECZ_RA, SPECZ_DEC: R.A. and decl.(in degrees) of the spec-*z*.
16. Column (194), SPECZ_SOURCE: the spectroscopic catalog listed in Table 5 that provides the spec-*z*.
17. Column (195), SED_BLAGN_FLAG: flag for BL AGN candidates identified in Appendix B. An entry of "1" stands for sources that are classified as BL AGN candidates by two different methods; "0.5" stands for sources identified as BL AGN candidates using one method but not the other; "0" indicates sources identified as non-BL AGNs by both methods.
18. Columns (196)–(197), PHOTOZ_RA, PHOTOZ_DEC: R.A. and decl. (in degrees) of the source in the forced-photometry catalog (K. Nyland et al. in 2021, in preparation), which includes forced photometry from DeepDrill, VIDEO, HSC, and VOICE that is utilized to compute photo-*z*s.
19. Column (198), PHOTOZ_BEST: photometric redshift adopted for the source. PHOTOZ_EAZY values are adopted for sources that have SED_BLAGN_FLAG < 1 and are not identified as BL AGNs in spectroscopic surveys, when PHOTOZ_EAZY_Q < 1; PHOTOZ_LEPHARE values are adopted for spectroscopically identified BL AGNs, SED_BLAGN_FLAG = 1 objects, and SED_BLAGN_FLAG = 0.5 objects with PHOTOZ_EAZY_Q ⩾ 1 (see Section 5.2 for details).
20. Columns (199)–(202), PHOTOZ_EAZY, PHOTOZ_EAZY_UERR, PHOTOZ_EAZY_LERR, PHOTOZ_EAZY_Q: photometric redshift computed by EAZY, the associated upper and lower uncertainties, and the photometric redshift quality parameter (Q_z).
21. Columns (203)–(205), PHOTOZ_LEPHARE, PHOTOZ_LEPHARE_UERR, PHOTOZ_LEPHARE_LERR: photometric redshift computed by LEPHARE and the associated upper and lower uncertainties. We only report LEPHARE photo-*z*s with $\chi^2_{red} < 2$ and band number > 10 (see Section 5.2 for details).
22. Column (206), AGN_FLAG: flag for AGNs identified in Section 6.
23. Column (207), STAR_FLAG: flag for stars identified in Appendix C.

Table 7: X-ray *source catalog in* ELAIS-S1

X-ray properties

Columns (1)–(110) give the X-ray properties of our sources in the same format as that of Table 6.

Multiwavelength properties

Columns (111)–(198) provide the multiwavelength properties of the matched counterparts with MATCH_FLAG = 1 utilizing NWAY.

1. Columns (111)–(113), P_ANY, P_I, FLAG_SECOND: see Columns (111)–(113) of Table 6.
2. Columns (114)–(119), IRAC_RA, IRAC_DEC, VIDEO_RA, VIDEO_DEC, DES_RA, DES_DEC: R.A. and decl. of the counterpart in the DeepDrill/VIDEO/DES catalog in degrees.
3. Columns (120)–(122), SEP_IRAC, SEP_VIDEO, SEP_DES: separation of the X-ray position from the DeepDrill/VIDEO/DES counterpart in arcseconds.
4. Columns (123)–(126), IRAC_1_MAG, IRAC_1_MAG_ERR, IRAC_2_MAG, IRAC_2_MAG_ERR: 1.9″ aperture photometry and uncertainties in the IRAC 3.6 μm and 4.5 μm bands reported in the DeepDrill catalog.
5. Columns (127)–(136), VIDEO_Z_MAG, VIDEO_Z_MAG_ERR, VIDEO_Y_MAG, VIDEO_Y_MAG_ERR, VIDEO_J_MAG, VIDEO_J_MAG_ERR, VIDEO_H_MAG, VIDEO_H_MAG_ERR, VIDEO_KS_MAG, VIDEO_KS_MAG_ERR: VIDEO 2″ aperture photometry and uncertainties in the *Z*, *Y*, *J*, *H*, and K_s bands.
6. Columns (137)–(146), DES_G_MAG, DES_G_MAG_ERR, DES_R_MAG, DES_R_MAG_ERR, DES_I_MAG, DES_I_MAG_ERR, DES_Z_MAG, DES_Z_MAG_ERR, DES_Y_MAG, DES_Y_MAG_ERR: DES Kron magnitude and uncertainties in the *g*, *r*, *i*, *z*, and *Y* bands.
7. Column (147), TRACTOR_ID: the object ID of the VIDEO counterpart in the forced-photometry catalog (Zou et al. 2021).
8. Columns (148)–(179), IRAC_1_FP_MAG, IRAC_1_FP_MAG_ERR, IRAC_2_FP_MAG, IRAC_2_FP_MAG_ERR, VIDEO_Z_FP_MAG, VIDEO_Z_FP_MAG_ERR, VIDEO_Y_FP_MAG, VIDEO_Y_FP_MAG_ERR, VIDEO_J_FP_MAG, VIDEO_J_FP_MAG_ERR, VIDEO_H_FP_MAG, VIDEO_H_FP_MAG_ERR, VIDEO_KS_FP_MAG, VIDEO_KS_FP_MAG_ERR, DES_G_FP_MAG, DES_G_FP_MAG_ERR, DES_R_FP_MAG, DES_R_FP_MAG_ERR, DES_I_FP_MAG, DES_I_FP_MAG_ERR, DES_Z_FP_MAG, DES_Z_FP_MAG_ERR, DES_Y_FP_MAG, DES_Y_FP_MAG_ERR, ESIS_B_FP_MAG, ESIS_B_FP_MAG_ERR, ESIS_V_FP_MAG, ESIS_V_FP_MAG_ERR, ESIS_R_FP_MAG, ESIS_R_FP_MAG_ERR, VOICE_U_FP_MAG, VOICE_U_FP_MAG_ERR: forced photometry and uncertainties of DeepDrill 3.6 μm and 4.5 μm bands, VIDEO *ZYJHK*$_s$ bands, DES *grizY* bands, ESIS *BVR* bands, and VOICE *u* band reported in the forced-photometry catalog (Zou et al. 2021).
9. Columns (180)–(198), SPECZ, SPECZ_CLASS, SPECZ_Q, SPECZ_RA, SPECZ_DEC, SPECZ_SOURCE, SED_BLAGN_FLAG, PHOTOZ_RA, PHOTOZ_DEC, PHOTOZ_BEST, PHOTOZ_EAZY, PHOTOZ_EAZY_UERR, PHOTOZ_EAZY_LERR, PHOTOZ_EAZY_Q, PHOTOZ_LEPHARE, PHOTOZ_LEPHARE_UERR, PHOTOZ_LEPHARE_LERR, AGN_FLAG, STAR_FLAG: see Columns (188)–(206) of Table 6.

Appendix B
Identifying BL AGN Candidates

Considering its X-ray sensitivity limit, the XMM-SERVS survey would be able to detect ≈95% of the spectroscopically identified BL AGNs in the COSMOS field (e.g., Marchesi et al. 2016), which is a survey field with rich spectroscopic observations.[52] As the sky density of spectroscopically confirmed BL AGNs (≈60 deg^{-2} for both W-CDF-S and ELAIS-S1) in our study is much less than that of COSMOS (≈290 deg^{-2}; Marchesi et al. 2016), we also identify BL AGN candidates in our X-ray catalogs that do not have spectroscopic classifications utilizing their SEDs via two independent methods: one method is based on machine learning, and the other is based on SED template fitting. As each of these methods has its own advantages and disadvantages, combining the results from both methods provides more reliable predictions for AGNs in our catalogs.

B.1. Machine-learning-based Classification

For X-ray sources in W-CDF-S and ELAIS-S1 that have both spectroscopic classifications and forced photometry, we use machine learning to assess the differences between the optical-to-IR SEDs of X-ray sources that are classified as BL AGNs (260 in W-CDF-S and 179 in ELAIS-S1) and X-ray sources that are not BL AGNs (470 in W-CDF-S and 333 in ELAIS-S1). Utilizing all the available photometric data points, we normalized the SEDs so that all the data points have a maximum value of 0 in log space, and we use the interp1d function in scipy to interpolate the log-space SED shape. We extract 16 data points at common observed-frame wavelengths from the interpolated SEDs (see Figure 30) to feed a 1D convolutional neutral network (CNN). Approximately 60% of the objects are used as the training set; ≈20% of the objects are used as the validation set; the remaining ≈20% of the objects are used as the test set. After training the network and selecting the best model utilizing the validation set, we could correctly predict ≈86% of the BL AGNs in the test set and ≈91% of the sources that are not BL AGNs in W-CDF-S (see Figure 31(a) for the confusion matrix). When we apply the trained model to the remaining X-ray sources in the W-CDF-S forced-photometry catalog with signal-to-noise ratio (S/N) > 3 detections in more than five bands, ≈790 (≈30%) of the sources are classified as BL AGN candidates. Combining these objects with the spectroscopically identified BL AGNs, the BL AGN density reaches ≈ 230 deg^{-2}. Considering that only ≈ 80% of the detected X-ray sources in W-CDF-S have reliably matched counterparts in the forced-photometry catalog (K. Nyland et al. 2021, in preparation) with S/N > 3 detections in more than five bands, this number is roughly consistent with the expectation from the COSMOS field. Similarly, after training the network in ELAIS-S1, we could correctly predict ≈80% of the BL AGNs and ≈ 85% of the sources that are not BL AGNs (see Figure 31(c)). About 450 (≈30%) of the remaining X-ray sources in the ELAIS-S1 forced-photometry catalog with S/N > 3 detections in more than five bands are classified as BL AGN candidates. The BL AGN density reaches ≈ 200 deg^{-2}. Considering that only ≈70% of the X-ray sources detected in ELAIS-S1 have S/N > 3 detections in more than five bands in

[52] As estimated in Section 2.1.3 of Yang et al. (2018), the fraction of BL AGNs missed by spectroscopic campaigns in the COSMOS field is likely less than ≈ 18%.

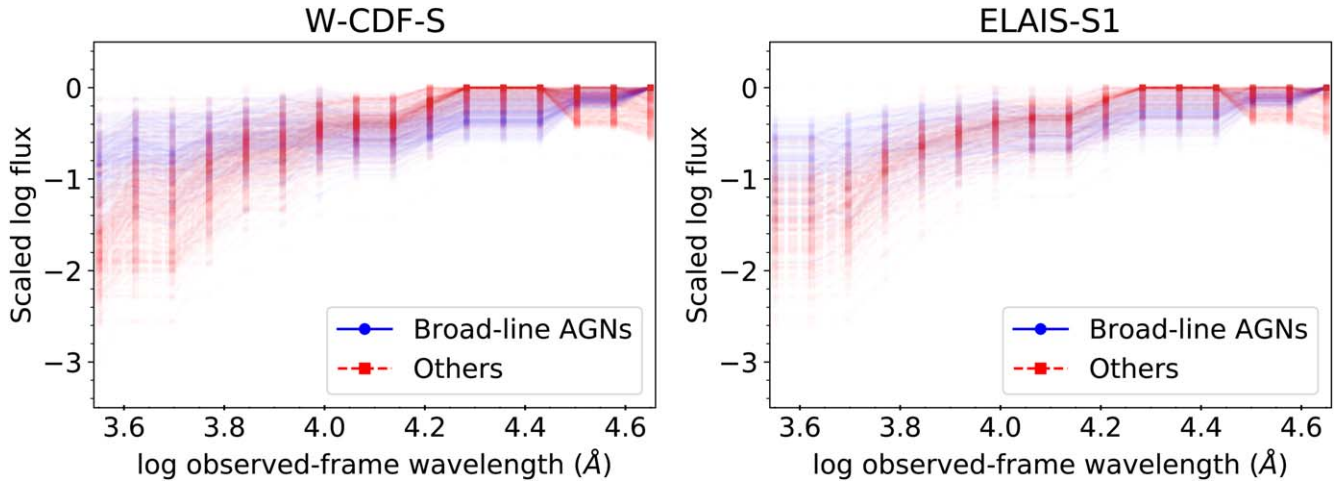

Figure 30. Extracted data points from the interpolated SEDs of BL AGNs identified in spectroscopic surveys (blue) compared with other X-ray sources that have spectroscopic classifications (red) in W-CDF-S (left) and ELAIS-S1 (right).

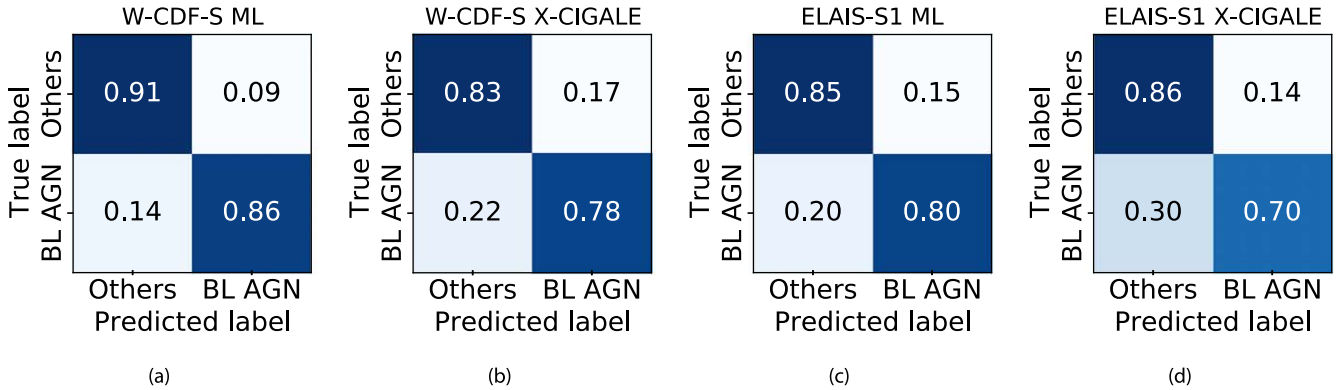

Figure 31. (a) The confusion matrix for the machine-learning-based classification of X-ray sources in W-CDF-S. (b) The confusion matrix for the X-CIGALE-based classification of X-ray sources in W-CDF-S. (c) The confusion matrix for the machine-learning-based classification of X-ray sources in ELAIS-S1. (d) The confusion matrix for the X-CIGALE-based classification of X-ray sources in ELAIS-S1.

the Zou et al. (2021) forced-photometry catalog (while this number is 80% for W-CDF-S), this relatively low BL AGN density is also acceptable.

B.2. SED-template-fitting-based Classification

We also utilize X-CIGALE (Yang et al. 2020) to identify BL AGNs from their optical-to-IR SEDs in combination with the X-ray flux level. We do not provide redshift information to X-CIGALE and allow X-CIGALE fit redshift as a free parameter. We adopt a delayed exponentially declining star formation history, a Chabrier initial mass function (Chabrier 2003), the extinction law from Calzetti et al. (2000), the dust emission template from Dale et al. (2014), the AGN component SKIRTOR (which is established based on Stalevski et al. 2012, 2016), and the X-ray module following Yang et al. (2020). Details of the fitting parameters are given in Table 8. As X-CIGALE requires intrinsic X-ray fluxes, we convert the observed X-ray flux derived in Section 3.5 to intrinsic absorption-corrected X-ray flux following the method in Section 4.4 of Luo et al. (2017). Basically, we assume that all X-ray sources with $\Gamma_{\rm eff} < 1.8$ suffer from some level of intrinsic absorption, and their intrinsic spectra have power-law shapes with a fixed photon index of 1.8. To identify AGNs, we utilized the ratio between the Bayesian estimation of the AGN 2–10 keV luminosity and the sum of the Bayesian estimation of the 2–10 keV LMXB luminosity and HMXB luminosity in the X-CIGALE output: if this ratio is greater than 10, we identify the source as an AGN. As BL AGNs generally do not suffer from high levels of extinction of the AGN emission, if the Bayesian estimation for the $E(B-V)$ parameter of the AGN component is smaller than 0.2, we classify the AGN as a BL AGN candidate. We tested the accuracy of the template-fitting-based classification utilizing X-ray sources that have spectroscopic classifications available; the confusion matrix can be seen in the relevant panels of Figure 31. We correctly predict ≈78% of the BL AGNs and ≈83% of the sources that are not BL AGNs in W-CDF-S; we correctly predict ≈70% of the BL AGNs and ≈86% of the sources that are not BL AGNs in ELAIS-S1. When we fit the remaining X-ray sources in the forced-photometry catalog that do not have spectroscopic classifications available, $\approx 690/350$ of the sources in W-CDF-S/ELAIS-S1 are classified as BL AGN candidates. As template fitting strongly relies on the number of photometric points available, the resulting BL AGN sky density ($\approx 210/180\,{\rm deg}^{-2}$ in W-CDF-S/ELAIS-S1) is roughly consistent with the expectation from the COSMOS field: only ≈65% of the X-ray sources in W-CDF-S and ELAIS-S1 without spectroscopic redshifts have $S/N > 3$ detections in at least 10 bands.

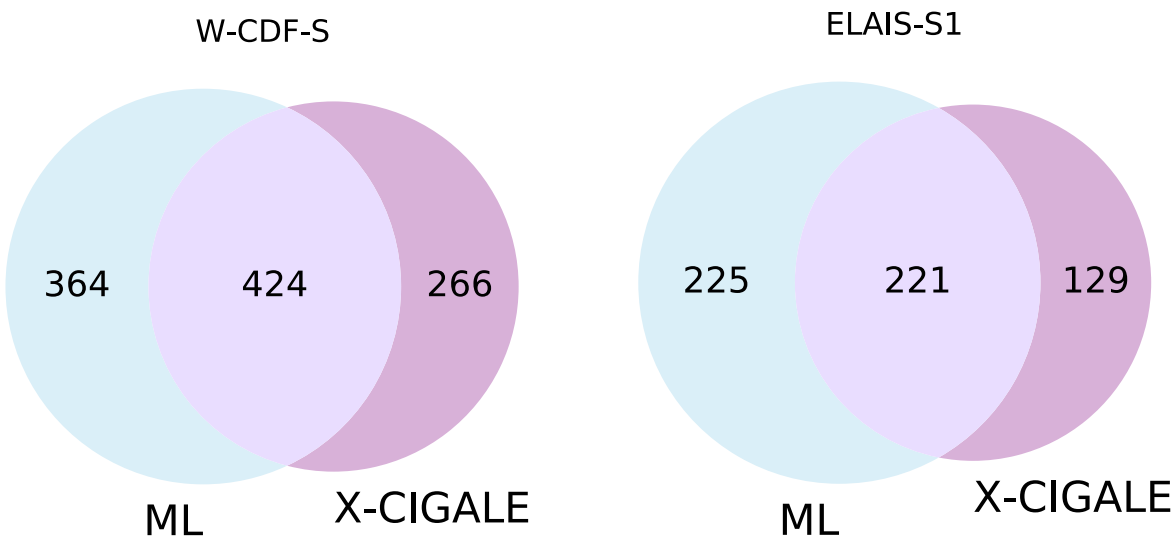

Figure 32. The Venn diagram for BL AGNs identified with the machine-learning-based approach and the X-CIGALE template-fitting-based approach.

Table 8
Utilized X-CIGALE Modules with Fitting Parameters

Module	Parameters	Values
Star formation history: *sfhdelayed*	τ (Myr)	100, 300, 500, 1000, 5000, 8000
	t (Myr)	100, 300, 500, 1000, 2000, 3000, 5000, 7000, 10000
Stellar population synthesis model: *bc03*	Initial mass function	Chabrier (2003)
Dust attenuation: *dustatt_calzetti*	$E(B-V)$	0.2–1.0 with steps of 0.1
Dust emission: *dale2014*	α in $dM_{\rm dust} \propto U^{-\alpha}{\rm d}U$	2.0
AGN emission: *skirtor2016*	Torus optical depth at 9.7 μm	7
	Viewing angle (deg)	30
	AGN fraction of total IR luminosity ($\rm frac_{AGN}$)	0–0.9 with steps of 0.1, and 0.99
	$E(B-V)$ of AGN polar dust	0–0.6 with steps of 0.1
X-ray	Γ	1.8
	$\max\lvert\Delta\alpha_{\rm OX}\rvert$	0.2

Note. Default values are adopted for parameters not listed.

B.3. Assessing the Reliability of BL AGN Candidates Identified

The above two methods each have advantages and disadvantages. The machine-learning-based method achieves a higher apparent level of accuracy; at the same time, as the model is trained based on BL AGNs with spectroscopic classifications (which are brighter compared with sources not identified in spectroscopic surveys), there might be biases associated with the predictions. While the template-fitting-based method does not suffer from the potential bias introduced from the training set, its accuracy is lower. Also, for both methods, the prediction accuracy declines when the available number of photometric data points is smaller. Thus, we create a flag, SED_BLAGN_FLAG, for the BL AGN candidates identified. SED_BLAGN_FLAG = 1 is assigned to $\approx 420/220$ X-ray sources in W-CDF-S/ELAIS-S1 that are identified as BL AGN candidates by both methods; SED_BLAGN_FLAG = 0.5 is assigned to $\approx 630/350$ X-ray sources in W-CDF-S/ELAIS-S1 that are identified as BL AGN candidates with one method but not the other (see Figure 32 for the Venn diagram).

To assess the reliability of the BL AGN candidates identified, we check the morphology and optical variability of BL AGN candidates identified in W-CDF-S. As luminous BL AGNs often appear to be pointlike sources when they dominate over host-galaxy starlight, morphological information has been adopted in selecting BL AGN candidates in some works (e.g., Salvato et al. 2009, 2011). In the HSC catalog presented in Ni et al. (2019), the sdss_pointlike flag selects pointlike sources with the SDSS algorithm, psfMag−CmodelMag < 0.145, in the reference band (the band in which the source is detected with the highest S/N). Utilizing this sdss_pointlike column, 1346 X-ray sources in W-CDF-S are considered to be pointlike through HSC morphology. Among 731 X-ray sources where spectroscopic classifications are available, HSC morphology could correctly classify $\approx 93\%$ of the BL AGNs and $\approx 82\%$ of the sources that are not BL AGNs. However, as HSC morphology becomes less accurate at higher redshift and fainter magnitudes, we only utilize it to assess the reliability of objects marked with SED_BLAGN_FLAG = 1 or = 0.5: although not all pointlike sources identified from HSC morphology are BL AGNs, we do expect a substantial fraction of the BL AGNs identified via SEDs to have sdss_pointlike = 1. Figure 33 shows that $\approx 64\%$ of the X-ray sources marked with SED_BLAGN_FLAG = 1 or = 0.5 in W-CDF-S are identified as pointlike sources utilizing HSC morphology. This fraction is $\approx 87\%$ for SED_BLAGN_FLAG = 1 sources and $\approx 48\%$ for SED_BLAGN_FLAG = 0.5 sources, suggesting that SED_BLAGN_FLAG = 1 is more reliable in identifying BL AGNs, as expected.

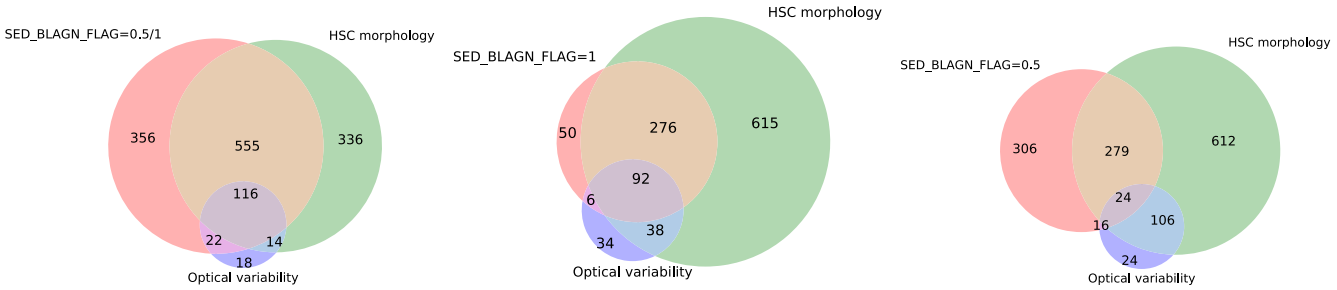

Figure 33. Left: the Venn diagram for the SED_BLAGN_FLAG = 1 or 0.5 sources, pointlike sources identified via HSC morphology, and reported optically variable sources in the W-CDF-S field. Middle: similar to the left panel, but for the SED_BLAGN_FLAG = 1 sources. Right: similar to the left panel, but for the SED_BLAGN_FLAG = 0.5 sources.

The catalogs of optically variable sources in W-CDF-S from Falocco et al. (2015) and Poulain et al. (2020) are also utilized to assess the quality of the BL AGN candidates selected from SEDs. A total of 333 of our X-ray sources in W-CDF-S are identified as potential AGNs in these catalogs (CLASS $\geqslant 0$), and these sources are likely to be BL AGNs. Approximately 160 of them have spectroscopic classification: $\approx$70% of them are real BL AGNs. Although the sample of BL AGN candidates identified via optical variability is incomplete and may have contamination (e.g., from supernovae or stars whose observed fluxes vary owing to internal or external reasons), it remains a useful sample for testing the completeness of BL AGNs identified via SEDs. As can be seen in Figure 33, SED_BLAGN_FLAG = 1 or = 0.5 objects in W-CDF-S include $\approx 81\%$ of the optically variable sources; SED_BLAGN_FLAG = 1 objects alone only include $\approx 58\%$ of the optically variable sources. Thus, the utilization of SED_BLAGN_FLAG = 1 alone will likely lead to a relatively incomplete BL AGN identification.

For the purposes of this work, we would like to provide reliable photo-z estimations for X-ray sources. About 70%/60% of the SED_BLAGN_FLAG = 1/0.5 objects in W-CDF-S and ELAIS-S1 do not have high-quality ($Q_z < 1$) EAZY photo-z measurements utilizing galaxy and obscured AGN templates (see Section 5.2). Thus, we use the AGN-dominated SED templates to fit all the SED_BLAGN_FLAG = 1 objects and all the SED_BLAGN_FLAG = 0.5 sources that cannot be characterized well (i.e., with $Q_z < 1$) by galaxy/obscured AGN templates (see Section 5.2).

Appendix C
Identifying Non-AGN X-Ray Sources

We have identified Galactic stars among non-AGN X-ray sources that are associated with reliable multiwavelength counterparts (see Section 6) based on the $g - z$ (or $B - z$) versus $z - K_s$ diagram in W-CDF-S (or ELAIS-S1); sources falling below the dashed line in Figure 34 are classified as stars. Figure 34 demonstrates that this criterion successfully identifies almost all of the spectroscopically confirmed stars. We also match the non-AGN X-ray sources to Gaia sources (e.g., Gaia Collaboration et al. 2018) with a matching radius of 1″ and classify sources with significant proper motions as stars. We visually examined the optical imaging to remove contaminating galaxies with obviously extended morphology. In total, 169 out of the 486 non-AGN X-ray sources in W-CDF-S are classified as stars; 92 out of the 345 non-AGN X-ray sources in ELAIS-S1 are classified as stars. For the remaining non-AGN X-ray sources, most are bright and large foreground galaxies (identified via visual examination) that contain a population of X-ray binaries and/or a low-luminosity AGN (see Figure 35 for example cutouts).

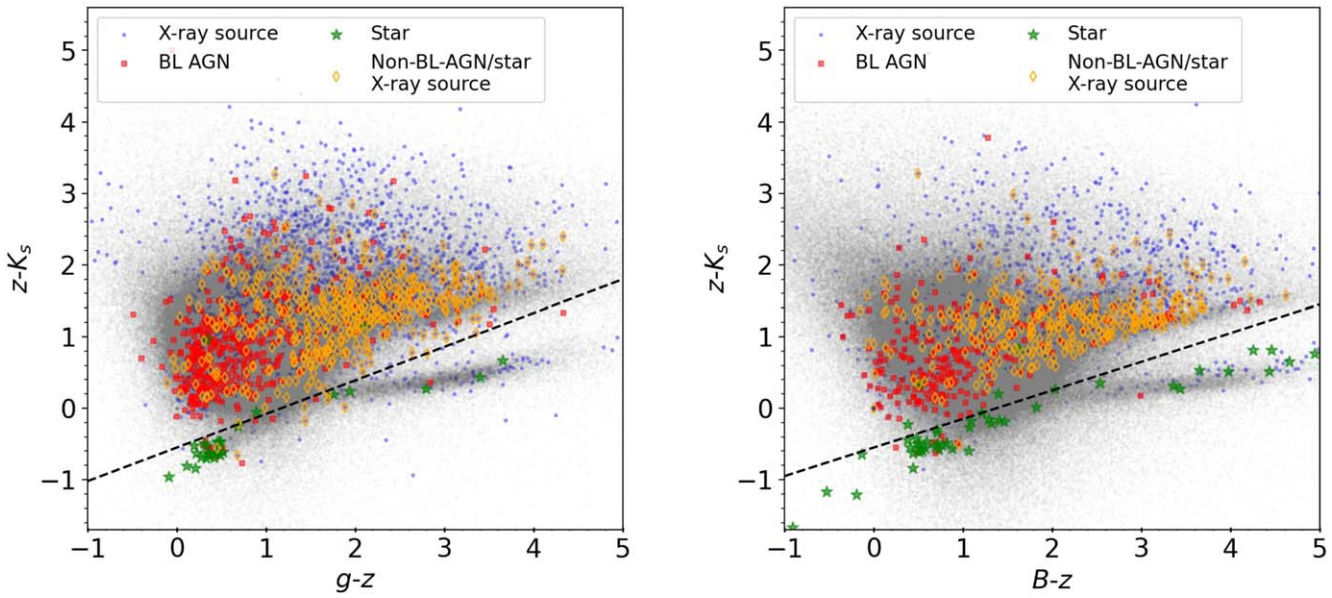

Figure 34. Left: the $g - z$ vs. $z - K_s$ diagram for sources in the W-CDF-S forced-photometry catalog (K. Nyland et al. 2021, in preparation) represented by the gray circles, which can be utilized to separate stars from other X-ray sources. X-ray sources are marked as blue circles; spectroscopically confirmed BL AGNs are indicated by red squares; spectroscopically identified stars are marked as green stars; X-ray sources with spectroscopic classification that are not identified as BL AGNs or stars are represented by orange diamonds. The black dashed line is utilized to identify stars among non-AGN sources. Right: the $B - z$ vs. $z - K_s$ diagram for sources in the ELAIS-S1 forced-photometry catalog (Zou et al. 2021). Symbols are similar to the top panel.

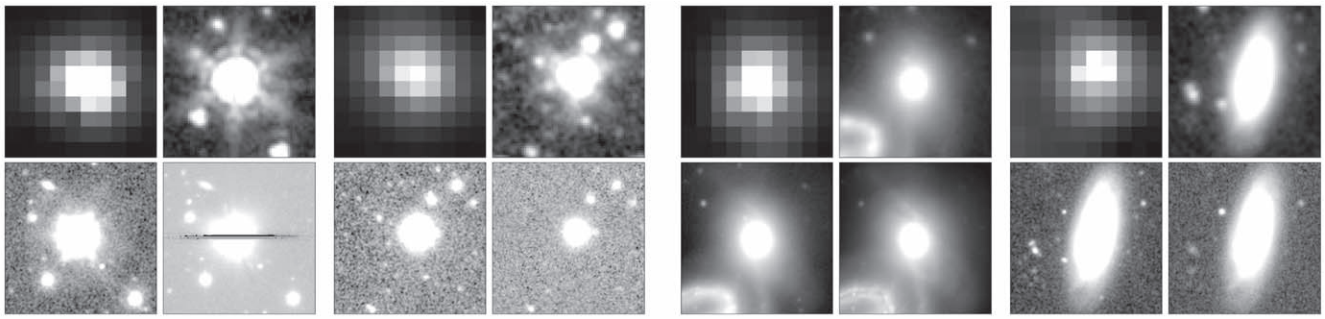

(a) (b) (c) (d)

Figure 35. Example multiwavelength cutouts of (a, b) X-ray-detected stars and (c, d) X-ray-detected galaxies in W-CDF-S/ELAIS-S1. Each panel shows four $40'' \times 40''$ cutouts: XMM-Newton 0.2–12 keV (top left), DeepDrill 3.6 μm band (top right), VIDEO K_s band (bottom left), and HSC (or DES) i band (bottom right).

ORCID iDs

Qingling Ni https://orcid.org/0000-0002-8577-2717
Chien-Ting Chen https://orcid.org/0000-0002-4945-5079
Bin Luo https://orcid.org/0000-0002-9036-0063
Guang Yang https://orcid.org/0000-0001-8835-7722
Fan Zou https://orcid.org/0000-0002-4436-6923
James Aird https://orcid.org/0000-0003-1908-8463
David M. Alexander https://orcid.org/0000-0002-5896-6313
Franz Erik Bauer https://orcid.org/0000-0002-8686-8737
Mark Lacy https://orcid.org/0000-0002-3032-1783
Bret D. Lehmer https://orcid.org/0000-0003-2192-3296
Mara Salvato https://orcid.org/0000-0001-7116-9303
Donald P. Schneider https://orcid.org/0000-0001-7240-7449
Paolo Tozzi https://orcid.org/0000-0003-3096-9966
Mattia Vaccari https://orcid.org/0000-0002-6748-0577
Cristian Vignali https://orcid.org/0000-0002-8853-9611
Fabio Vito https://orcid.org/0000-0003-0680-9305
Yongquan Xue https://orcid.org/0000-0002-1935-8104
Andrea Comastri https://orcid.org/0000-0003-3451-9970
Roberto Gilli https://orcid.org/0000-0001-8121-6177
James Mullaney https://orcid.org/0000-0002-3126-6712
Maurizio Paolillo https://orcid.org/0000-0003-4210-7693
Axel Schwope https://orcid.org/0000-0003-3441-9355
Ohad Shemmer https://orcid.org/0000-0003-4327-1460
Mouyuan Sun https://orcid.org/0000-0002-0771-2153
John D. Timlin III https://orcid.org/0000-0001-8131-1801
Jonathan R. Trump https://orcid.org/0000-0002-1410-0470

References

Abazajian, K. N., Adelman-McCarthy, J. K., Agüeros, M. A., et al. 2009, ApJS, 182, 543
Abbott, T. M. C., Adamow, M., Aguena, M., et al. 2021, ApJS, 255, 20
Aird, J., Coil, A. L., Georgakakis, A., et al. 2015, MNRAS, 451, 1892
Alexander, D. M., Bauer, F. E., Chapman, S. C., et al. 2005, ApJ, 632, 736
Ananna, T. T., Salvato, M., LaMassa, S., et al. 2017, ApJ, 850, 66
Arnouts, S., Cristiani, S., Moscardini, L., et al. 1999, MNRAS, 310, 540
Berta, S., Rubele, S., Franceschini, A., et al. 2006, A&A, 451, 881

Brammer, G. B., van Dokkum, P. G., & Coppi, P. 2008, ApJ, 686, 1503
Brandt, W. N., & Alexander, D. M. 2015, A&ARv, 23, 1
Brandt, W. N., Ni, Q., Yang, G., et al. 2018, arXiv:1811.06542
Broos, P. S., Townsley, L. K., Feigelson, E. D., et al. 2011, ApJS, 194, 2
Calzetti, D., Armus, L., Bohlin, R. C., et al. 2000, ApJ, 533, 682
Cappelluti, N., Brusa, M., Hasinger, G., et al. 2009, A&A, 497, 635
Chabrier, G. 2003, PASP, 115, 763
Chen, C. T. J., Brandt, W. N., Luo, B., et al. 2018, MNRAS, 478, 2132
Chiappetti, L., Fotopoulou, S., Lidman, C., et al. 2018, A&A, 620, A12
Civano, F., Marchesi, S., Comastri, A., et al. 2016, ApJ, 819, 62
Coil, A. L., Blanton, M. R., Burles, S. M., et al. 2011, ApJ, 741, 8
Colless, M., Dalton, G., Maddox, S., et al. 2001, MNRAS, 328, 1039
Comastri, A., Ranalli, P., Iwasawa, K., et al. 2011, A&A, 526, L9
Cooper, M. C., Yan, R., Dickinson, M., et al. 2012, MNRAS, 425, 2116
Dale, D. A., Helou, G., Magdis, G. E., et al. 2014, ApJ, 784, 83
Davies, L. J. M., Robotham, A. S. G., Driver, S. P., et al. 2018, MNRAS, 480, 768
Donley, J. L., Koekemoer, A. M., Brusa, M., et al. 2012, ApJ, 748, 142
Donley, J. L., Rieke, G. H., Rigby, J. R., & Pérez-González, P. G. 2005, ApJ, 634, 169
Driver, S. P., Liske, J., Davies, L. J. M., et al. 2019, Msngr, 175, 46
Driver, S. P., & Robotham, A. S. G. 2010, MNRAS, 407, 2131
Eales, S., Chapin, E. L., Devlin, M. J., et al. 2009, ApJ, 707, 1779
Evans, I. N., Primini, F. A., Glotfelty, K. J., et al. 2010, ApJS, 189, 37
Falocco, S., Paolillo, M., Covone, G., et al. 2015, A&A, 579, A115
Feruglio, C., Fiore, F., La Franca, F., et al. 2008, A&A, 488, 417
Franzen, T. M. O., Banfield, J. K., Hales, C. A., et al. 2015, MNRAS, 453, 4020
Gaia Collaboration, Brown, A. G. A., Vallenari, A., et al. 2018, A&A, 616, A1
Ilbert, O., Arnouts, S., McCracken, H. J., et al. 2006, A&A, 457, 841
Jarvis, M., Taylor, R., Agudo, I., et al. 2016, arXiv:1709.01901
Jarvis, M. J., Bonfield, D. G., Bruce, V. A., et al. 2013, MNRAS, 428, 1281
Jones, D. H., Read, M. A., Saunders, W., et al. 2009, MNRAS, 399, 683
Kelson, D. D., Williams, R. J., Dressler, A., et al. 2014, ApJ, 783, 110
Kim, M., Wilkes, B. J., Kim, D.-W., et al. 2007, ApJ, 659, 29
Klypin, A., Yepes, G., Gottlöber, S., Prada, F., & Heß, S. 2016, MNRAS, 457, 4340
Kollmeier, J. A., Zasowski, G., Rix, H.-W., et al. 2017, arXiv:1711.03234
Lacy, M., Storrie-Lombardi, L. J., Sajina, A., et al. 2004, ApJS, 154, 166
Lacy, M., Surace, J. A., Farrah, D., et al. 2021, MNRAS, 501, 892
LaMassa, S. M., Georgakakis, A., Vivek, M., et al. 2019, ApJ, 876, 50
LaMassa, S. M., Urry, C. M., Cappelluti, N., et al. 2016, ApJ, 817, 172
Lang, D., Hogg, D. W., & Mykytyn, D. 2016, The Tractor: Probabilistic Astronomical Source Detection and Measurement v1.0, Astrophysics Source Code Library, ascl:1604.008
Lanzuisi, G., Civano, F., Elvis, M., et al. 2013, MNRAS, 431, 978
Levi, M., Allen, L. E., Raichoor, A., et al. 2019, BAAS, 51, 57
Lidman, C., Tucker, B. E., Davis, T. M., et al. 2020, MNRAS, 496, 19
Liu, T., Merloni, A., Simm, T., et al. 2020, ApJS, 250, 32
Liu, T., Tozzi, P., Wang, J.-X., et al. 2017, ApJS, 232, 8
Liu, Z., Merloni, A., Georgakakis, A., et al. 2016, MNRAS, 459, 1602
Lonsdale, C. J., Smith, H. E., Rowan-Robinson, M., et al. 2003, PASP, 115, 897
Luo, B., Brandt, W. N., Xue, Y. Q., et al. 2017, ApJS, 228, 2
Maiolino, R., Cirasuolo, M., Afonso, J., et al. 2020, Msngr, 180, 24
Mao, M. Y., Sharp, R., Norris, R. P., et al. 2012, MNRAS, 426, 3334
Marchesi, S., Civano, F., Elvis, M., et al. 2016, ApJ, 817, 34
Marshall, F. E., Boldt, E. A., Holt, S. S., et al. 1980, ApJ, 235, 4
Martin, D. C., Fanson, J., Schiminovich, D., et al. 2005, ApJL, 619, L1
Mauduit, J. C., Lacy, M., Farrah, D., et al. 2012, PASP, 124, 714
Menzel, M. L., Merloni, A., Georgakakis, A., et al. 2016, MNRAS, 457, 110
Monet, D. G., Levine, S. E., Canzian, B., et al. 2003, AJ, 125, 984
Moster, B. P., Somerville, R. S., Newman, J. A., & Rix, H.-W. 2011, ApJ, 731, 113
Nandra, K., Laird, E. S., Aird, J. A., et al. 2015, ApJS, 220, 10
Ni, Q., Timlin, J., Brandt, W. N., & Yang, G. 2019, RNAAS, 3, 5
Nyland, K., Lacy, M., Sajina, A., et al. 2017, ApJS, 230, 9
Oliver, S. J., Bock, J., Altieri, B., et al. 2012, MNRAS, 424, 1614
Pierre, M., Pacaud, F., Adami, C., et al. 2016, A&A, 592, A1
Pineau, F. X., Derriere, S., Motch, C., et al. 2017, A&A, 597, A89
Poulain, M., Paolillo, M., De Cicco, D., et al. 2020, A&A, 634, A50
Puccetti, S., Fiore, F., D'Elia, V., et al. 2006, A&A, 457, 501
Ranalli, P., Comastri, A., Vignali, C., et al. 2013, A&A, 555, A42
Rosen, S. R., Webb, N. A., Watson, M. G., et al. 2016, A&A, 590, A1
Sacchi, N., La Franca, F., Feruglio, C., et al. 2009, ApJ, 703, 1778
Salvato, M., Buchner, J., Budavári, T., et al. 2018, MNRAS, 473, 4937
Salvato, M., Hasinger, G., Ilbert, O., et al. 2009, ApJ, 690, 1250
Salvato, M., Ilbert, O., Hasinger, G., et al. 2011, ApJ, 742, 61
Scolnic, D. M., Lochner, M., Gris, P., et al. 2018, arXiv:1812.00516
Shirley, R., Roehlly, Y., Hurley, P. D., et al. 2019, MNRAS, 490, 634
Silverman, J. D., Mainieri, V., Salvato, M., et al. 2010, ApJS, 191, 124
Skrutskie, M. F., Cutri, R. M., Stiening, R., et al. 2006, AJ, 131, 1163
Stalevski, M., Fritz, J., Baes, M., Nakos, T., & Popović, L. Č. 2012, MNRAS, 420, 2756
Stalevski, M., Ricci, C., Ueda, Y., et al. 2016, MNRAS, 458, 2288
Stern, D., Eisenhardt, P., Gorjian, V., et al. 2005, ApJ, 631, 163
Swann, E., Sullivan, M., Carrick, J., et al. 2019, Msngr, 175, 58
Thorne, J. E., Robotham, A. S. G., Davies, L. J. M., et al. 2021, MNRAS, 505, 540
Traulsen, I., Schwope, A. D., Lamer, G., et al. 2019, A&A, 624, A77
Traulsen, I., Schwope, A. D., Lamer, G., et al. 2020, A&A, 641, A137
Ueda, Y., Akiyama, M., Hasinger, G., Miyaji, T., & Watson, M. G. 2014, ApJ, 786, 104
Ueda, Y., Watson, M. G., Stewart, I. M., et al. 2008, ApJS, 179, 124
Vaccari, M. 2015, in Proc. of Science 267, The Many Facets of Extragalactic Radio Surveys: Towards New Scientific Challenges (Trieste: Sissa), 27
Vaccari, M., Covone, G., Radovich, M., et al. 2016, in Proc. of Science 275, 4th Annual Conf. on High Energy Astrophysics in Southern Africa (HEASA 2016) (Trieste: Sissa), 26
Vito, F., Brandt, W. N., Yang, G., et al. 2018, MNRAS, 473, 2378
Webb, N. A., Coriat, M., Traulsen, I., et al. 2020, A&A, 641, A136
Willingale, R., Starling, R. L. C., Beardmore, A. P., Tanvir, N. R., & O'Brien, P. T. 2013, MNRAS, 431, 394
Xue, Y. Q. 2017, NewAR, 79, 59
Xue, Y. Q., Luo, B., Brandt, W. N., et al. 2011, ApJS, 195, 10
Xue, Y. Q., Luo, B., Brandt, W. N., et al. 2016, ApJS, 224, 15
Yang, G., Boquien, M., Buat, V., et al. 2020, MNRAS, 491, 740
Yang, G., Brandt, W. N., Luo, B., et al. 2016, ApJ, 831, 145
Yang, G., Brandt, W. N., Vito, F., et al. 2018, MNRAS, 475, 1887
Zou, F., Brandt, W. N., Lacy, M., et al. 2021, RNAAS, 5, 31
Zou, F., Yang, G., Brandt, W. N., et al. 2021, RNAAS, 5, 56